Chapter 2
Charge Transport and Recombination in Organic Solar Cells (OSCs)

Nanjia Zhou and Antonio Facchetti

2.1 Basic Concepts of Charge Transport in Organic Semiconductors

Organic compounds are mainly hydrocarbon compounds with a backbone of carbon atoms. The strong bonds that form the molecular backbone are a result of overlap of sp^2 hybridized atomic orbitals of adjacent carbon atoms, yielding a bonding σ and an antibonding σ^* orbitals. The remaining unhybridized p orbitals overlap and form π and π^*orbitals. The energies of π orbitals are higher than those of σ orbitals, whereas energies of π^* orbitals are lower than those of σ orbitals. Based on Pauli exclusion principle and Hund's rule, the energies of π and π^* orbitals are defined as highest occupied molecular orbital (HOMO), and lowest unoccupied molecular orbitals (LUMO), respectively.

For charge transport to take place in organic solids, there must be a charge on the molecular unit. This may either be an additional electron that is accommodated in an antibonding orbital, or one that is removed from bonding orbital. The molecule is then no longer in the ground state but rather in a charged excited state.

There are a number of factors that can influence charge carrier mobilities, including molecular packing, disorder, temperature, impurities, electric field, and pressure [1].

N. Zhou (✉)
Department of Materials Science and Engineering,
Northwestern University, 2220 campus Drive, Evaston, IL 60208, USA
e-mail: nanjiazhou@u.northwestern.edu

A. Facchetti
Department of Chemistry, Northwestern University,
2145 Sheridan Road, Evanston, IL 60208, USA
e-mail: a-facchetti@northwestern.edu

H. Huang, J. Huang (eds.), *Organic and Hybrid Solar Cells,*
DOI 10.1007/978-3-319-10855-1_2

2.1.1 General Approach to Charge Transfer Mechanisms

For inorganic semiconductors such as silicon (Si) and germanium (Ge), which involve covalent bonds with high-bonding energy, charge carriers move as highly delocalized plane waves and carrier mobilities are often far larger than 1 cm^2/Vs. In these systems, as a result of carrier scattering, increasing temperature reduces the carrier mobilities. On the other hand, in the case for organic semiconductors, they consist of π-conjugated units and they are kept together mainly by weak van der Waals forces with weak bonding energies on the same order as molecular vibrational energies at room temperature. In addition, the separations between molecules are sufficiently large for molecular orbitals to overlap. Therefore, charge transport in organic semiconductors takes place in the form of hopping mechanism. In contrast to inorganic semiconductors, elevated temperature increases the charge carrier mobilities for organic semiconductors. Understanding the fundamental charge transport mechanisms at both molecular and device levels are of special importance to organic semiconductors. There are several excellent review articles to cover this topic. For example, interested readers can find these recent reviews regarding charge transport in organic semiconductors [1, 2].

Typically, it is believed that semiconductors with carrier mobilities higher than 1 cm^2/Vs involve carrier transport via delocalized plane waves, whereas carrier mobilities less than 0.1 cm^2/Vs are suggestive of hopping conduction between localized states across different molecules. For hopping transport, the relationship between carrier mobility and temperature follows Eq. (2.1).

$$\mu = \mu_0 \exp\left[-\left(\frac{T_0}{T}\right)^{\frac{1}{\alpha}}\right], \alpha \text{ is between 1 and 4.} \tag{2.1}$$

The exact charge transport mechanisms in organic semiconductors are still under debate. The most commonly used model is the Holstein's small-polaron model [3]. In covalent π-conjugated organic systems, the distribution of electronic cloud in molecules is highly delocalized. Self-trapping occurs via the creation of localized states in the gap between conduction band and valence band, which results in the formation of polarons. The Holstein model simplifies the charge transport as a 1D, one-electron model. The total energy in the system consists of three elements: (i) lattice energy E_L which is a sum of N number of harmonic oscillator at a single frequency, ω_0, in the form of:

$$E_L = \sum_{n=1}^{N} \frac{1}{2M}\left(\frac{\hbar}{i}\frac{\partial}{\partial u_n}\right) + \frac{1}{2} M \omega_0^2 u_n^2 \tag{2.2}$$

where u_n is the displacement of nth molecule from its equilibrium position and M is the reduced mass of each molecular site; (ii) the energy dispersion of the electron which can be written in the form of:

$$E_k = E_0 - 2J\cos(ka) \tag{2.3}$$

where J is the electron transfer energy and a is the lattice constant; (iii) the electron-lattice coupling in the form of $\varepsilon_n = -Au_n$, where A is a constant.

Another important parameter to consider is the polaron-binding energy, E_b, which is described as the energy gain of an infinitely slow carrier due to polarization and deformation. It can be described as:

$$E_b = A^2 / (2M\omega_0^2) \tag{2.4}$$

When electronic bandwidth, $2J$, is smaller than E_b, the small-polaron model faces its limit. In such condition, the electronic term of the total Hamiltonian can be treated as a small perturbation, and the mobility of the small polaron can be described as a time-dependent Schrödinger equation. At high temperature ($T > \Theta$, Θ is the Debye temperature), mobility is obtained through:

$$\mu = \sqrt{\frac{\pi}{2}} \frac{ea^2}{\hbar} \frac{J^2}{\sqrt{E_b}} (kT)^{-\frac{3}{2}} \exp\left(-\frac{E_b}{2kT}\right) \tag{2.5}$$

where $\frac{ea^2}{\hbar}$ has the dimension of a carrier mobility, and is close to 1 cm^2/Vs for most organic crystals.

It is also worth noting that at high field ($> 10^5$ V/cm), the carrier transport in organic materials is field-dependent. This is because the external field can alter the columbic potentials near localized-energy levels, thus increasing the electron tunnel transfer rate between sites. This phenomenon is described as Poole–Frankel mechanism. The field-dependent mobility, $\mu(F)$, can be described as:

$$\mu(F) = \mu(0) \exp\left(\frac{q}{kT} \beta \sqrt{F}\right) \tag{2.6}$$

Where $\mu(0)$ is the mobility at zero field, and β is the Poole–Frankel constant, which can be obtained from:

$$\beta = \left(\frac{e}{\pi\varepsilon\varepsilon_0}\right)^{\frac{1}{2}} \tag{2.7}$$

Where ε is the dielectric constant and ε_0 is the vacuum dielectric constant [3].

The multiple trapping and release (MTR) model is most widely used in describing charge transport in amorphous silicon. MTR model assumes that: (i) the probability of carrier arriving at a trap site and being trapped is close to unity; (ii) the release of trapped carrier is a thermally activated process. The relationship between drift mobility, μ_D and the mobility in the delocalized band, μ_0, can be described as:

$$\mu_D = \mu_0 \alpha \exp\left(-\frac{E_t}{kT}\right) \tag{2.8}$$

Where E_t is the energy difference between trap and band edge of delocalized band, and α is the ratio between the effective density of states at delocalized band–band edge to the concentration of traps.

Various other models have been employed for describing charge transport in organic semiconductors [4–6]. For example, Borsenberger et al. [4] described the charge transport in disordered molecular solids in the form of hopping transport between the Gaussian DOS of hopping sites. Meijer et al. [6] in the studies of pentacene and α-hexathiophene, discovered that the carrier transport follows Meyer–Neldel rule (MNR), in which the carrier transport mobility can be described as:

$$X = X_{00} \exp - E_a \left(\frac{1}{k_B T} - \frac{1}{E_{MN}} \right) \tag{2.9}$$

Where E_{MN} is the Meyer–Neldel energy, and E_a is the activation energy.

2.2 Operation of Organic Photovoltaic (OPV)

In this section, some basics of OPV are outlined. First, the fundamentals of photovoltaic effect known from conventional semiconductor models are outlined. Then, equivalent circuit models widely used for describing different solar cell systems are presented. Next, we outline the unique processes occurred in OPVs and the origins of V_{OC}, J_{SC}, and fill factor (FF) are described. Last, we focus on the two types of recombination dynamics, geminate and nongeminate recombination, which are the two dominating loss mechanisms limiting the performance of OPVs.

2.2.1 Photovoltaic Effect

2.2.1.1 Photon Absorption

The basic relationship between photon wavelength, λ, and energy is:

$$\lambda = \frac{C}{\nu} = \frac{hC}{h\nu} = \frac{1.24}{h\nu} \ (\mu m) \tag{2.10}$$

where C is the speed of light in vacuum, ν is the frequency of light, h is Planck's constant.

When a semiconductor interacts with incident light, photons can be absorbed under these circumstances: (i) when $h\nu = E_g$ electrons are activated from the valence band to the conduction band; (ii) when $h\nu > E_g$, in addition to the formation of electron-hole pair, the excess energy $h\nu - E_g$ is released in the form of heat; (iii) when $h\nu < E_g$, the photons can be absorbed only if there exist deep level states as a result of chemical impurities or physical defects.

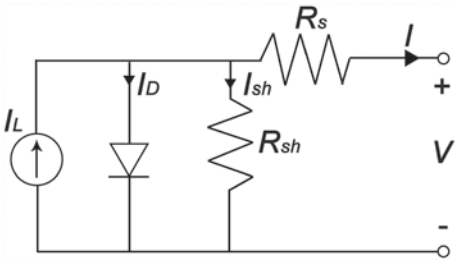

Fig. 2.1 Equivalent circuit of a practical solar cell

2.2.1.2 Semiconductor Photovoltaic Effect and Charge Transport Equations

The transport of electrons and holes in inorganic semiconductors can be described using field current and diffusion current. The one-dimensional drift-diffusion equation follows:

$$J_n = q\mu_e n\frac{\partial E_c}{\partial x} + qD_n\frac{\partial n}{\partial x} \tag{2.11}$$

$$J_p = q\mu_h p\frac{\partial E_v}{\partial x} - qD_p\frac{\partial p}{\partial x} \tag{2.12}$$

Where $J_{e,h}$, is the electron/hole current density, $\mu_{e,h}$ is the electron/hole mobilities, and $D_{e,h}$ is the electron/hole diffusion coefficients. Assuming an electric field $E=-grad\varphi$ and uniform distribution of electrons and holes, the total charge, j_Q, can be written as:

$$j_Q = \frac{\sigma_e}{e}grad\eta_e - \frac{\sigma_e}{e}grad\eta_e \tag{2.13}$$

For conventional *pn*-junction solar cells, the space charge forms a stable electric field in the direction of *n*-type toward *p*-type, with the diffusion voltage being:

$$\psi_0 = \psi_n - \psi_p = V_T ln\frac{N_d N_a}{n_i^2} \tag{2.14}$$

Where N_a is the majority carrier concentration, N_d is the donor impurity concentration, n_i is the intrinsic carrier concentration, and V_T is the thermoelectric field.

2.2.2 Solar Cell Equivalent Circuit Model

For an ideal solar cell, the I–V characteristics can be described using equivalent circuit (Fig. 2.1):

When ignoring the effect of series resistance (R_s) and shunt resistance (R_{sh}) ($R_s = 0$ and $R_{sh} = \infty$) for ideal solar cell, current can be represented by the difference between short circuit photocurrent, I_L, and the forward current of *pn*-junction, or dark current,

$$I_D = \left(1 - e^{\frac{V}{V_T}} \right) \tag{2.15}$$

$$I = I_L - I_D = I_L + I_0 \left(1 - e^{\frac{V}{V_T}} \right) \tag{2.16}$$

where I_0 is the saturation current. Therefore, the voltage on *pn*-junction is given by:

$$V = V_T \ln \left(1 + \frac{I_L - I}{I_0} \right) \tag{2.17}$$

Under short-circuit condition ($V = 0$), the current output is the short-circuit current: $I = I_L = I_{sc}$ Whereas under open-circuit condition ($I = 0$), the open-circuit voltage is given by:

$$V_{oc} = V_T \ln \left(1 + \frac{I_L}{I_0} \right). \tag{2.18}$$

Based on the equivalent circuit diagram of solar cell, the solar cell output power is given simply by:

$$P = IV = (I_L - I_D)V = I_L V + I_0 V \left(1 - e^{\frac{V}{V_T}} \right) \tag{2.19}$$

To further include the discussion of R_s and R_{sh} for practical solar cells, the I–V characteristics are modified from ideal solar cell condition:

$$I = I_L + I_0 \left(1 - \frac{e\left(V - IR_s\right)}{V_T} \right) - \frac{V - IR_s}{R_{sh}} \tag{2.20}$$

The power conversion efficiency (PCE) is represented by the ratio between solar cell maximum power output, P_m, and input power from incident light, P_{in}:

$$\eta = \frac{P_m}{P_{in}} \times 100\% \tag{2.21}$$

Here, according to Eq. 2.19, P_m can be further represented as:

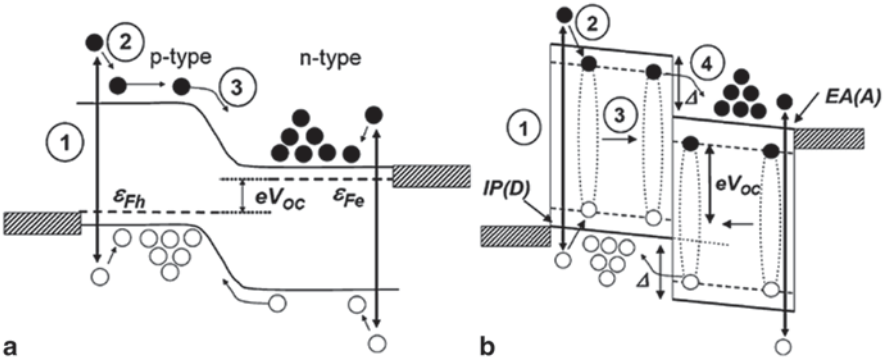

Fig. 2.2 Comparison of the typical energy diagrams of **a** an inorganic solar cell and **b** an organic solar cells. **a** In inorganic *p-n* junction solar cells, absorption of photon energy leads to thermalization of the holes and electrons near the top of the valence and conduction bands (*step 1*), followed by the diffusion of minority carriers to the junction (*step 2*) and they are eventually swept away and accumulate on the other side of the junction where they become the majority carriers (*step 3*). V_{oc} of *p-n* junction solar cells is determined by the difference between the quasi-Fermi level energies of *n*-and *p*-type semiconductors (denoted as ε_{Fe} and ε_{Fh}, respectively). **b** In organic solar cells, absorption of photons (*step 1*) lead to the formation of a bound electron-hole pair, exciton, (*step 2*) which diffuse to the donor/acceptor interface (*step 3*). As a result of energy difference between electron affinity of the donor and the acceptor materials, excitons can dissociate and form free-charge carriers (*step 4*). In this process, the maximum V_{oc} is determined between ionization potential of donor (*IP*(*D*)) and electron affinity of acceptor (*EQ*(*A*)). Reproduced from ref [7]

$$P_m = V_{mP} I_{mP} = \frac{{V_{mP}}^2 I_L}{V_{mP} + V_T}\left(1 + \frac{I_0}{I_L}\right) \tag{2.22}$$

where V_{mP} and I_{mP} are the voltage and current at the maximum power point per unit area. It is obvious that high solar cell efficiency requires high I_{sc} and V_{oc}. Another important factor, FF also contributes to the solar cell efficiency. FF is defined as the ratio between P_m and the product of V_{oc} and I_{sc} : $FF = \frac{V_{mP} I_{mp}}{V_{oc} I_{sc}}$. Finally, according to Eq. 2.21, the PCE is therefore defined as:

$$\eta = \frac{V_{oc} \times I_{sc} \times FF}{P_{in}}$$

2.2.3 Organic Photovoltaic Cells

In the simple picture of an energy diagram, a p-type semiconductor and an n type semiconductor is placed adjacent to each other, forming an abrupt interface. (Fig. 2.2) Different from traditional *p-n* junction type solar cells, in OPV operation, the absorption of a photon does not directly lead to a free electron and a free hole.

This entity in which electron and hole are still bound to each other by Coulomb forces is called an exciton, and it requires a relatively large driving force to be separated [1].

The basic light absorption process in OPV can be simply summarized as following: charge pairs are generated throughout the device with the generation rate proportion to the optical absorption profile $Q(x)$, calculated as [8]

$$Q(x) = \frac{1}{2} c\varepsilon_0 \alpha n \left| E(x) \right|^2 \tag{2.23}$$

where c is vacuum speed of light, ε_0 is the vacuum permittivity, n is the refractive index, α is the absorption coefficient. Charge-pair separation efficiency is then determined via the Onsager–Braun formula that depends on the local strength of the internal electrical field (see more further).

Another important property of OPV active layer is that they are macroscopically homogeneous mixtures and cannot differentiate charge transport direction without selective contacts. Usually, a combination of a low-work function and a high-work function electrode, as well as common *n*-type and *p*-type interfacial layers are used to differentiate electron and hole transport. A standard model for charge collection in bulk heterojunction (BHJ) OPV is illustrated in a recent review by Bisquert et al. [9]. In principle, the transport of separated charges to the electrodes can be modeled via drift-diffusion equations as described previously with the additional possibility of the trapping and detrapping of electrons from deep trap states. In the following sections, the exciton dissociation and charge collection processes involving two key recombination mechanisms: geminate recombination and nongeminate recombination will be discussed in more details.

2.2.4 Basic Charge Transport Expressions in Organic Solar Cells

Similar to inorganic-type solar cells described previously, the fundamental relationship between charge and electric field can be described by Poisson's equation:

$$\frac{dE}{dx} = \frac{\rho}{\varepsilon} = \frac{q}{\varepsilon}(p(x) - n(x) + N_D - N_A) \tag{2.24}$$

At any given position x in solar cell photoactive layer, the exciton-generation rate (the number of exciton generated) can be represented as:

$$G(x) = \frac{Q(x)}{E_e} = \frac{Q(x)}{h\nu} = Q(x)\frac{\lambda}{hc} \tag{2.25}$$

where $E_e = \frac{hc}{\lambda}$ is the exciton energy,

where E is the electric field, ρ is the charge density and ε is the material permittivity. The electron and hole continuity equations are:

$$\frac{1}{q}\frac{dJ_n(x)}{dx} + G(x) - R(x) = 0 \tag{2.26}$$

$$\frac{1}{q}\frac{dJ_p(x)}{dx} + G(x) - R(x) = 0 \tag{2.27}$$

At any given position x in solar cell photoactive layer, the short-circuit current density $J(x)$ is the difference between carrier generation rate and recombination rate.

2.2.5 Origin of V_{oc}, J_{sc}, and FF

2.2.5.1 V_{oc}

V_{oc} of OPV is a result of splitting electron and hole quasi-Fermi energy levels triggered by illumination.

$$V_{oc} = \frac{1}{q}(E_{Fn} - E_{Fp}) \tag{2.28}$$

Where E_{Fn} and E_{Fp} are the electron and hole quasi-Fermi energies, respectively. Scharber et al. [10] summarized a series of OPV active layers and propose the empirical relationship between the HOMO of the donor materials and LUMO of the acceptors, proposed by Scharber et al.,

$$V_{oc} = \frac{1}{q}(E_{HOMO,D} - E_{LUMO,A} - 0.3V) \tag{2.29}$$

It should be noted that the V_{oc} loss of 0.3 eV is empirical, and the loss could be greater or smaller.

There are a number of factors that can adversely affect the V_{oc} of OPV devices. Consideration on disorder-induced V_{oc} loss and carrier recombination induced V_{oc} loss, V_{oc} can be expressed: [11]

$$qV_{oc} = \Delta E_{DA} - \frac{\sigma^2}{k_B T} - k_B T \ln\left(\frac{N_A N_D}{np}\right) \tag{2.30}$$

In Eq. 2.30, the first term is the effective bandgap, ΔE_{DA}, the second term is the disorder-induced V_{oc} loss, and the third term represents carrier recombination induced V_{oc} loss.

Experimentally, the dependence of V_{oc} on temperature and light intensity has profound effect on identifying basic OPV properties. By linearly fit V_{oc} with respect to temperature, it was found that $V_{OC} = \Delta E_{DA}$ when T approaches 0 K [12, 13]. However, this linear dependence is only valid at low temperature. V_{oc} was rather

found to saturate at elevated temperatures and started to decrease at certain temperature. This effect can be easily simulated according to Eq. 2.30 [11]. Therefore, by measuring V_{oc} saturation experimentally, one can estimate the degree of disorder in OPVs.

The steady-state light intensity dependence of V_{oc} is widely used to fit to a logarithmic relationship:

$$V_{oc} = S\ln(I / I_0), \tag{2.31}$$

where I_0 is the light intensity under 1 sun condition [14–16]. Here the slope, S, can be compared to nkT/q, where n is the ideality factor. For p-n junction-based inorganic solar cells, n is often observed to be close to 1 since bimolecular recombination is the predominant loss mechanism. Whereas $n > 1.5$ is often found in several OPV systems [7, 17], indicating the presence of possible other recombination mechanisms, i.e., trap-assisted recombination.

2.2.5.2 J_{sc}

J_{sc} is directly related to the spectral response, and it can be simply calculated by integrating the external-quantum efficiency, η_{EQE}, against the AM 1.5G spectrum. (where $N_{ph}(\lambda)$ is the photon flux density at wavelength (λ))

$$J_{sc} = \int_{AM\,1.5} e\eta_{EQE}(\lambda)N_{ph}(\lambda)d\lambda \tag{2.32}$$

Where E is the photon energy, q is the elementary charge [7].

Similar to V_{oc}, light intensity dependent J_{sc} measurement is also good indicator of recombination orders [18].

2.2.5.3 FF

Unlike V_{oc} and J_{sc} which can be estimated relatively easily through material-energetic alignment of D and A, i.e., lowering optical bandgap to maximize J_{sc}, while lowering the HOMO energies of donor materials to increase V_{oc}. Note, however, that HOMO lowering will also increase the bandgap, underscoring the problematic tradeoff between V_{oc} and J_{sc}. Realizing high FFs has proven elusive, although there is evidence that carrier mobility, active-layer microstructure, and also interfacial and bulk charge recombination play a role [19, 20].

After solving equivalent circuit model, a common expression for ideal FF_0 (no resistance considered) can be written as:

$$FF_0 = \frac{\tilde{v}_{oc} - \ln(\tilde{v}_{oc} + 0.72V)}{\tilde{v}_{oc} + 1} \tag{2.33}$$

where $\tilde{v}_{oc}$ is the normalized V_{oc},

$$\tilde{v}_{oc} = \frac{V_{oc}}{n_{id} kT / q}, \tag{2.34}$$

where k is the Boltzmann constant, T is temperature, q is the magnitude of the electrical charge on the electron, and n_{id} is an ideality factor relating to an ideal ($n_{id}=1$) or nonideal ($n_{id}>1$) diode [21]. OPVs typically have ideality factors in the range 1.5–2 due to their inherent disorder [7], and departures from unity are attributed to various recombination mechanisms inside band-to-band transitions, that is, trap-assisted and tail-state recombination [7].

It is well known that FF directly relates to carrier recombination, which reduces carrier lifetime and therefore the current extractable from the device. Factors limiting FF are widely discussed as a field-dependent competition between nongeminate recombination and charge extraction, with trap states and departure from diode ideality playing important roles [22, 23]. At high internal electric fields or near short-circuit conditions, enhanced bulk-charge mobility can improve transport and reduce space charge buildup. However, at low-internal fields or near V_{oc}, long carrier lifetimes determine charge extraction and thus the steepness of the J–V curve [23, 24]. Accordingly, both carrier mobility and lifetime are target parameters to enhance which can lead to increased FFs [25]. FF and J_{sc} could be limited by buildup of space charge, brought about by a large difference in the hole and electron mobility. While complexity of FF includes consideration of many factors, a simple explanation of the shape of J-V curves can be described through diode model, using variable R_s and R_{sh}. Specifically, R_s has a pronounced effect on the shape of J-V curves near V_{oc}, whereas R_{sh} has predominant effect near J_{sc}. After considering R_s, R_{sh}, and n, FF can be generally expressed as: [26]

$$FF = FF_s \left(1 - \frac{\tilde{v}_{oc} + 0.7}{\tilde{v}_{oc}} \frac{FF_s}{r_{sh}} \right) \tag{2.35}$$

where

$$FF_s = FF_0 0(1 - 1.1 r_s) + \frac{r_s}{5.4} \tag{2.36}$$

Servateis et al. [27] simulated the J-V response of P3HT:PC_{61}BM cell using different R_s parameters according to Shockley equation: (Fig. 2.3)

$$J = J_0 \left[\exp\left(\frac{e(V - JR_s)}{nk_B T} \right) - 1 \right] + \frac{V - JR_s}{R_p} - J_L \tag{2.37}$$

It was found that R_s can significantly impact FF, while not dramatically affect V_{oc}. R_s can be further influenced by both intrinsic properties of devices such as mobility,

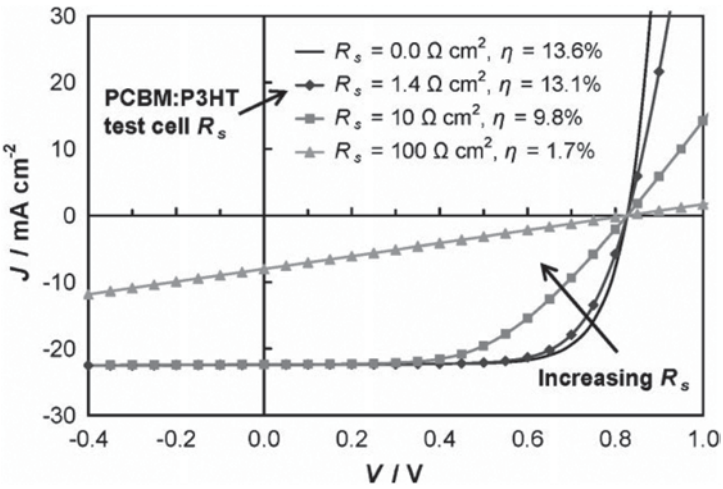

Fig. 2.3 The effect of R_s variation on projected *J-V* characteristics for the P3HT:$PC_{61}BM$ test cell. These data assume that R_s is the only parameter that changes; all other parameters in Eq. 2.37 are held constant (i.e., J_L, R_p, n, and J_o). (Reproduced from ref [27])

and carrier concentration, as well as external parameters such as cell dimensions and electrode resistance. R_{sh}, on the other hand, can be influenced by surface morphology between active layers and interfacial layers. Furthermore, the current leakage from pinholes in the film should be avoided to obtain high R_{sh}.

For high-quality monocrystalline inorganic solar cells, FFs greater than 80 % are routine. However, for typical high-performance OPV, FF is often found to be in the range of 65–75 %, mainly caused by a number of recombination mechanisms. Marks and coworkers recently reported OPV with unprecedently high FF of close to 80 % [17]. They attributed the high FF to a combination of factors: the design of highly ordered, closely packed, and properly oriented active-layer microstructures with optimal horizontal phase separation and vertical phase gradation.

2.2.6 Geminate and Nongeminate Recombination

2.2.6.1 Geminate Recombination

Organic solar cells combine both *p*-type and *n*-type semiconductors with the *p*-type material showing higher electron affinity and ionization potential than the *n*-type. In this regard, the photoexcited exciton needs to be dissociated at the DA interface to create charge carriers. The complete model of the electronic processes in OPV is depicted in Fig. 2.4. In principle, excitons diffuse to the D/A interface with a formation of geminate pair intermediates. If the geminate pairs dissociate, the carriers can transport through the structure and may be collected at the electrodes; otherwise,

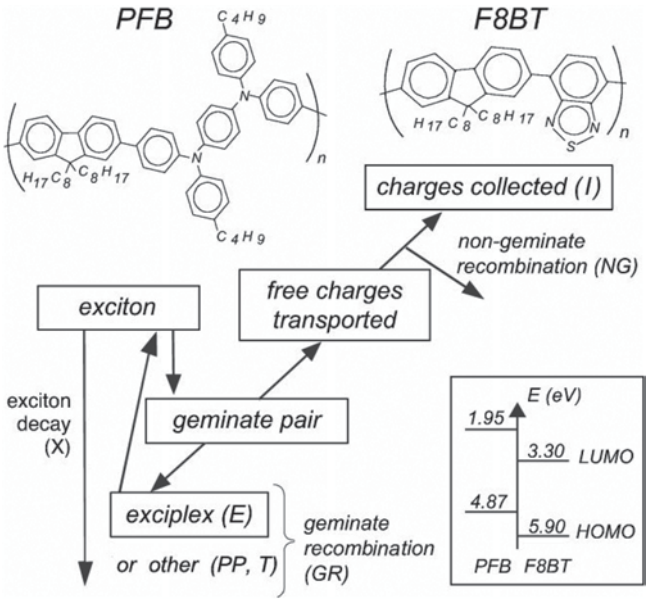

Fig. 2.4 Chemical structures of a donor/acceptor system with *PFB* and *F8BT* forming a type II heterojunction, and a simple illustration of basic OPV processes involving charge carrier formation and recombination. Exciton can either decay (depicted as *X*) or can reach the heterojunction to form geminate pairs. These can either be trapped (forming exciplexes (*E*), dark polaron pairs (*PP*) or triplets (*T*)) or separate into charges to be transported and collected at the electrodes (*I*). During this process, nongeminate recombination (*NG*) might occur. (Reproduced from ref [28])

they will undergo geminate recombination process wich can be a major loss mechanism in OPV.

For geminate recombination, electron and hole must overcome their mutual Coulumb attraction, or so called exciton binding energy, which can be written as:

$$E_C = \frac{e^2}{4\pi\varepsilon_r\varepsilon_0 r} \tag{2.38}$$

where e is the elemental charge, ε_r is the relative dielectric constant of the surrounding media, ε_0 is the vacuum permittivity, and r is the electron-hole pair separation distance. Comparing the inorganic semiconductors which typically have $\varepsilon_r > 10$ and E_C on the order of 10 meV, organic semiconductors typically have ε_r between 2 and 4, and (Tex translation failed) . This impose a serious challenge for exciton dissociation since the thermal energy at room temperature, $kT = 0.025$ eV, which makes it impossible that the thermal activation can be responsible for exciton dissociation to overcome a huge energy barrier.

Despite a century of research on charge-separation models, the exact mechanisms of exciton dissociation in OPV are yet to be clarified. Among the theoretical modeling works, Onsager–Braun theory is the most commonly used approach for

describing the exciton dissociation processes in disordered organic semiconductors [29]. Onsager described the exciton dissociation mechanism as a drift/diffusion process under a mutual Coulomb attraction and external-electric field [30]. Braun extended the Onsager theory in 1984 by introducing the finite lifetime for bound state of exciton [31]. It is worth to note that the Onsager–Braun theory still face limitations such as it doesn't consider hopping transport and spatial disorder [32].

It is found that highly-efficient geminate pair dissociation can be explained by delocalized charge carriers within conjugated segments of polymer chain [32]. Furthermore, geminate recombination can be influenced by charge trapping [33], energetic disorder of broadened density of states for HOMO and LUMO, delocalized charge transfer (CT) states, morphology and energy cascades. These factors are well discussed in two recent articles by Groves et al. [34, 35].

To experimentally differentiate geminate and nongeminate recombination remains to be challenging. In principle, when geminate recombination is a dominant recombination mechanism, the exciton separation typically can follow bias dependence, whereas in the case for nongeminate recombination, the initial mobile charge density is independent of voltage [18, 36].

2.2.6.2 Nongeminate Recombination

Nongeminate recombination is widely believed to be the major recombination mechanisms. Nongeminate recombination are bimolecular, mainly Langevin-type [37–40], and Shockley–Read–Hall (SRH)-type trap-assisted recombination, involving energy states or tail states within the bandgap [41, 42].

For Langevin-type, the recombination is based on the diffusion equation of charge carriers of opposite sign toward each other in the mutual electric field, and the transport rate is given by Langevin equation:

$$\beta = \frac{e(\mu_e + \mu_h)}{\varepsilon\varepsilon_0} \tag{2.39}$$

where e is the elementary charge, ε_0 is the vacuum permittivity, and μ_e and μ_h are the electron and hole mobilities, respectively [2].

In principle, Langevin equation assumes ambipolar transport. However, the Langevin recombination constants are frequently found experimentally to deviate from theoretical values, sometimes, by a large degree. This deviation can be attributed to larger domains, increasing energetic disorder and larger mismatch between the electron and hole mobility. Wetzelaer et al. [43] included the Langevin prefactor γ_{pre} in the Langevin equation:

$$k_R = \gamma_{pre} k_L = \gamma_{pre} \frac{q}{\varepsilon}(\mu_p + \mu_e) \tag{2.40}$$

where k_R is the total recombination strength.

In systems where mid-gap traps are present, free carriers are captured and released by trap states, causing the so-called trap assisted recombination. For SRH model, the carrier trapping, de-trapping and recombination follows the following rate equation:

$$\frac{\delta n_t}{\delta t} = r_{ec} - r_{ee} - r_{hc} + r_{he} \tag{2.41}$$

where r_{ec} and r_{hc} are the rates at which free electrons or holes get trapped, r_{ee} is the rate at which electrons can escape from the trap back to free-electron population, r_{he} is the rate at which holes escape back to the free-hole population.

Nongeminate recombination is often studied by a variety of techniques, including steady-state measurement and transient electrical measurement using a pulsed laser to create a population of charge carriers at a discrete instant in time then probing the evolution of that population by either an optical pulse or time-varying electrical field. Some of these measurements will be discussed in more details below.

2.3 Development of Carrier Transport and Recombination Measurement for OPV Cells

With progress in optical and electrical techniques in providing physical understanding of device operation, the charge collection processes of BHJ solar cells can be relatively well explained. From here on, this chapter will focus on the development of carrier transport and recombination measurement on the device or bulk scale.

2.3.1 Time-of-Flight (TOF)

In organic semiconductors and optoelectronic devices, charge mobilities can be determined experimentally by various techniques [1]. We briefly describe below the basic principles of some of the most widely referenced methods and recent progresses of investigation on charge transport and recombination mechanisms in OPV and related devices.

The TOF measurement has been widely used in a variety of optoelectronic devices to measure the real-time charge transport mobility [44]. The measurement usually starts with a short pulse of incident light and allows the collection of field-driven drift of electrons to acquire the transient photocurrent response of a material. It should be noted that this measurement is typically performed under very high fields ($> 10^5$ Vcm^{-1}) that are precipitously close to dielectric breakdown conditions, and where depletion region covers the entire device thickness. Therefore, these measurements are typically operated different than actual device operating conditions [45].

The charge carrier mobility is calculated using the equation: $\mu = d^2 / t_{tr} U$, where d is the film thickness, t_{tr} is the transit time, and U is the external voltage. In the study of nongeminate recombination in OPV, the Langevin recombination coefficient, β_L, is proportional to the charge carrier mobility, via $\beta_L = e(\mu_p + \mu_e) / \varepsilon\varepsilon_0$ [46, 47], while the TOF is only generating a single value for β that is valid for a particular set of conditions (charge density and extraction time). Clarke et al. [48–50] used resistance-dependent TOF technique to identify the non-Langevin bimolecular recombination. Thus allows the extraction of the ratio between bimolecular recombination coefficient, β, and the Langevin recombination coefficient:

$$\frac{\beta}{\beta_L} = \frac{CU_0}{Q_e} \frac{t_{tr}}{t_e} \tag{2.42}$$

where C is the capacitance of the system, and Q_e is the extracted charge.

TOF measurement has been used to study the charge transport characteristics both in neat materials and blend films [47, 51]. For example, recently, Hoffmann et al. [52] investigated the relationship between HOMO energies of polymers and TOF mobilities, and discovered an exponential decrease in mobilities with higher-lying HOMO energies. The high-hole mobilities in systems with low-lying HOMOs are due to the combined effect of disorderness and hole localization present in polymers. TOF measurements have also been successfully employed for study charge transport and recombination in active layer blend films. Mauer et al. [53, 54] used TOF method to study both hole and electron charge transport in P3HT:$PC_{61}BM$ blends. They found the regioregular P3HT exhibits a mobility of $\sim 5 \pm 10^{-5}$ cm^{-2} V^{-1} s^{-1}, which can well balance with that of $PC_{61}BM$. Howard et al. [55] further demonstrated in this system that the 3D Langevin recombination rate γ_{3D}, can be extracted by measuring TOF mobility. By comparing the thermally unannealed and annealed blend samples, they found γ_{3D} is slower in annealed sample ($1.9 \pm 0.3 \times 10^{-20}$) vs. unannealed sample ($2.3 \pm 0.5 \times 10^{-15}$).

Another way of quantifying charge sweep-out dynamics can be through optical TOF experiment by using a bias dependent TA setup [56]. The carrier mobility can be extracted from carrier sweep-out time.

2.3.2 Field Effect Transistor

The operation mechanisms of organic field-effect transistors (OTFT) can be described differently for enhancement mode field-effect transistor (FET) and the depletion mode FET. The basic principle of OTFT follows Poisson equation:

$$\frac{d^2 V(x)}{dx^2} = -\frac{\rho(x)}{\varepsilon_0 \varepsilon_i} \tag{2.43}$$

where V is the voltage between gate dielectric, ρ is the electron density, ε_0 and ε_s are the vacuum and semiconductor dielectric constants. The basic principles of OTFT follow the device physics of their inorganic predecessors. Source drain current is written as:

$$I_{SD} = \frac{W}{L}\mu C_i \left\{ \left(V_G - 2\phi_b - \frac{V_{SD}}{2} \right) V_{SD} - \frac{2}{3} \frac{\sqrt{2\varepsilon_i q N_a}}{C_i} \left[\left(V_{SD} + 2\phi_b \right)^{\frac{3}{2}} - \left(2\phi_b \right)^{\frac{3}{2}} \right] \right\} \quad (2.44)$$

where unit capacitor of dielectric layer $C_i = \varepsilon_i / d$, W is the channel width and L is the channel length, μ is the carrier mobility, V_G is the gate voltage and V_{SD} is the source-drain voltage, ϕ_b is the difference between Fermi energy and material intrinsic energy, ε_i is dielectric constant of the semiconductor, N_a is the doping concentration.

When V_{SD} is small, Eq. 2.44 can be simplified to:

$$I_{SD} = \frac{W}{L}\mu C_i (V_G - V_T) V_{SD} \quad (2.45)$$

where V_T is the threshold voltage. Under small V_{SD}, I_{SD}, and V_{SD} follows linear relationship. Here, V_T can be expressed as:

$$V_T = 2\phi_b + \frac{\sqrt{2\varepsilon_i q N_a (2\phi_b)}}{C_i} \quad (2.46)$$

When I_{SD} reaches saturation, I_{SD} can be expressed as:

$$I_{SD} = \frac{W}{2L}\mu C_i (V_G - V_T)^2 \quad (2.47)$$

In typical OFET measurement, charges migrate within a very narrow channel at the interface between the semiconducting layer and the dielectric. Here, a number of factors can have significant influences on the charge transport characteristics: surface polarity, traps/defects at the interface, contact resistance at the source and drain metal/organic interfaces, and dielectric constants of the gate material.

OTFT measurement is one of the most universally employed measurement techniques for characterizing charge transport properties for organic semiconductor devices. It is also well-known that a number of molecular self-assembly parameters can significantly affect the electronic structure and charge transport in the π-conjugated organic semiconductors [57–59].

To mimic the OPV active layer, ambipolar organic thin-film transistors are often fabricated [51, 57, 58, 60–64]. Hauff et al. [65] reported an electron mobility of the order of 10^{-3} cm^2 V^{-1} s^{-1} in pure PCBM films. However, upon blending with P3HT, they reported a decrease in the electron mobility by an order of magnitude, which was attributed to the unoptimized morphology of the blend film.

Lombardo et al. [66] demonstrated the output and transfer plots for both *p*-channel and *n*-channel FET modes, and the resistor characteristic measured at dark and illuminated conditions. By combining the recombination rate and continuity equa-

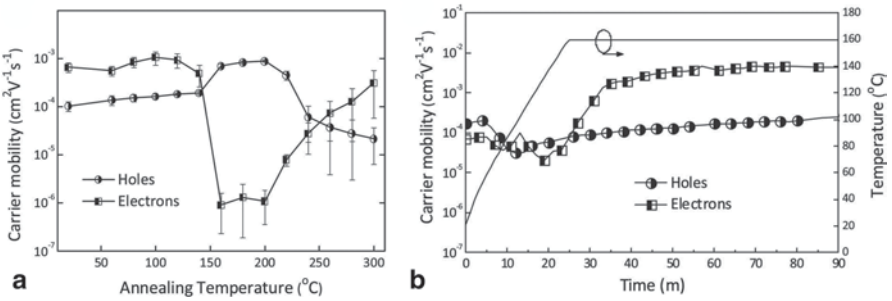

Fig. 2.5 **a** Average saturation-regime field-effect mobility of holes and electrons in four 1:1 (wt%) P3HT:$PC_{71}BM$ blend ambipolar BCBG OFET measured at room temperature under ambient pres-sure in N_2 after being annealed in various temperature after 30 min. **b** Saturation-regime field-effect mobility of holes and electrons in a 1:1 (wt%) P3HT:$PC_{71}BM$ blend ambipolar BGBC OFET measured as a function of time, whilst being annealed at 160 °C. Reproduced from ref [67]

tion, the bimolecular recombination constant can be calculated to be 1.7×10^{-14} for P3HT:PCBM devices.

Labram et al. [67] also probed the morphology evolution of P3HT:$PC_{61}BM$ and P3HT:$PC_{71}BM$ films by characterizing blend based transistors using a bottom-contact, bottom-gate (BCBG) architecture (Fig. 2.5). They observed that in the P3HT:$PC_{71}BM$ films, hole mobility is enhanced by a factor of 3.5 whereas the reduction of electron mobility falls by a factor of 500 when the active layer is annealed at 160 °C. This indicates that the percolation of $PC_{71}BM$ can be dramatically influenced by thermal annealing. The hole mobility started to fall whereas electron mobility increases at 200 °C annealing, this indicates the redistribution of fullerene molecules. Zhang et al. [64] studied the photoresponse of two organic bulk heterojunction type transistors using a bottom-gate, top-contact configurations: P3HT:$PC_{71}BM$ and a high-performance small molecule 3,6-bis(5-(benzofuran-2-yl)thiophen-2-yl)-2,5-bis(2-ethylhexyl)pyrrolo[3,4-c]pyrrole-1,4-dione ($DPP(TBFu)_2$):$PC_{71}BM$ system. It was found that *p*-type and *n*-type mobilities can be well balanced in P3HT:$PC_{71}BM$ systems, whereas the $DPP(TBFu)_2$:$PC_{71}BM$ system shows considerably lower *p*-type than *n*-type mobilities. They concluded that this could be a result of less-efficient charge separation assisted by electric fields after exciton dissociation.

2.3.3 Space Charge Limited Current (SCLC)

While organic semiconductors have been typically characterized in a FET configuration, SCLC technique has also been widely used for a variety of organic semiconductors for a long history [46, 68, 69]. In principle, organic semiconductors are generally disordered, trap-free, and having unbalanced low mobilities. It is also worth noting that comparing to TFT which measures the charge transport characteristics

in direction horizontal to the substrate, SCLC measurement provides the advantage of measuring it in the direction perpendicular to substrate. This clearly is advantageous in simulating actual OPV operation conditions. Therefore, SCLC has been most widely used by synthetic chemists to characterize mobilities either for the neat semiconductors and blends [70–75].

In SCLC configuration, either hole-only or electron-only devices are fabricated for measuring *p*-type or *n*-type semiconductors, respectively. For *p*-type materials, usually a configuration of ITO/*p*-type semiconductor/high work function metal is used, whereas for *n*-type materials, a configuration of ITO/*n*-type semiconductor/low work function metal is used. In both cases, metal electrodes are the injection electrodes. With assumption of Ohmic contact at both interfaces and correcting for contact resistance, the charge injection current is only limited by the ideal trap-free electrical resistance. Due to the charge accumulation at the electrode, a space charge is formed and an electric field which tends to prevent the injection of new charge carriers is created.

According to Mott–Gurney relationship, assuming negligible number of deep localized states and field dependent mobility, the SCLC current density in the device is given by:

$$J_{sclc} = \frac{9}{8}\varepsilon_0 \varepsilon_r \mu \frac{V_{in}^{\ 2}}{L^3} \tag{2.48}$$

where ε_0 is the vacuum permittivity, ε_r is the relative dielectric constant of active layer, μ is the charge carrier mobility, L is the thickness of the device, and V_{in} is the voltage dropped across the device:

$$V_{in} = V - V_{bi} - V_{rs} \tag{2.49}$$

where V is the applied voltage, V_{bi} is the built-in voltage and V_{rs} is the voltage dropped due to the series resistance.

In a variety of OPV systems, SCLC mobilities are particularly useful techniques in describing carrier transport characteristics of active layer materials [37, 68, 70, 76–79]. Bartelt et al. [80] investigated the inclusion of PCBM on decreasing hole mobilities of donor polymers, as well as the thickness dependence transport characteristics of both neat and blend films. Zhou et al. [81] investigated the SCLC mobilities of all-polymer blends (PTB7:N2200) when processed using different solvents, and discovered that the hole mobilities of n-type polymers in these all-polymer blends are severely impeded by percolation with the *n*-type polymers. Faist et al. [82] studied the SCLC electron mobilities of varies D/A combinations, and discovered that high-crystalline materials such as P3HT show high SCLC mobilities when combining with mono- and multi-adduct fullerenes, whereas less crystalline polymers such as PCDTBT shows low mobilities. Similarly, Azimi et al. [78] also concluded that the significantly lowered electron mobility in Si-PCPDTBT:bis-PCBM is a main cause for its lowered OPV performance (Fig. 2.6).

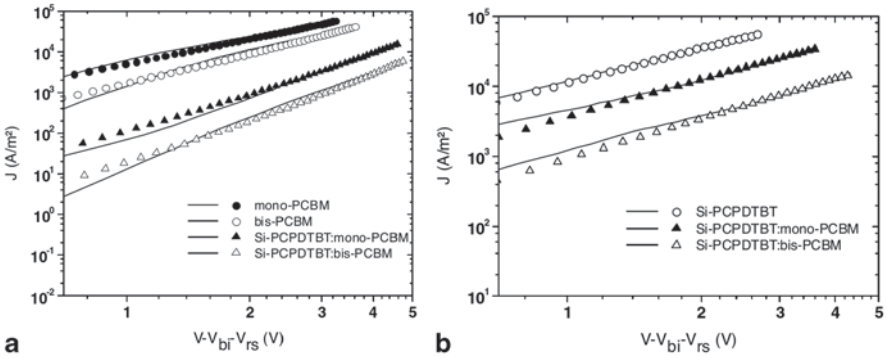

Fig. 2.6 *J-V* characteristics of **a** electron-only and, **b** hole-only device for pristine mono-PCBM and bis-PCBM and for the blend of Si-PCPDTBT with mono-PCBM and bis-PCBM under the dark condition. The symbols denote for the fit using a model of space charge limited current with the field-dependent mobility. (Reproduced from ref [78])

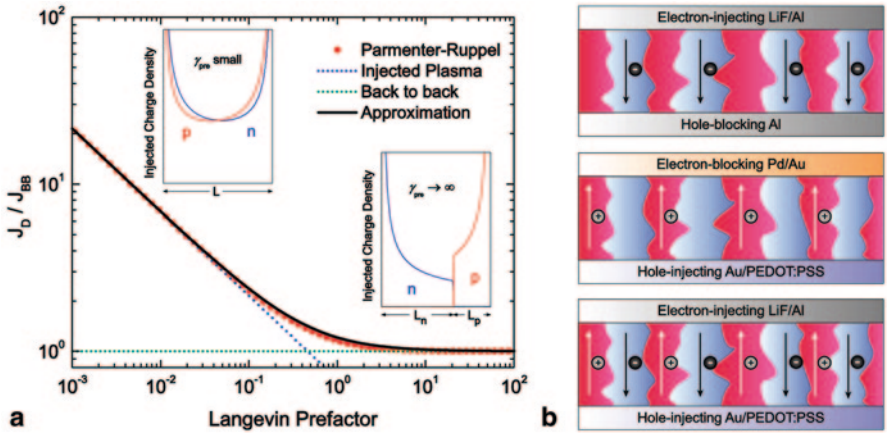

Fig. 2.7 **a** Normalized double-carrier current density as a function of the Langevin prefactor. The double-carrier current density is normalized by the current density at infinite recombination, which equals the sum of the electron and hole current densities. The insets show the injection-carrier distribution across the film for slow (*left*) and infinite (*right*) recombination, calculated from drift-diffusion model. **b** Illustration of double injection devices. Schematic representation of the three types of devices: electron-only, hole-only, and double-carrier device. The bottom electrodes are biased positively, while the top electrodes are biased negatively (forward bias). (Reproduced from ref [43])

Weitzelaer et al. [43] reported a novel steady-state technique to extract the bimolecular recombination constants γ_{pre} without the need for transient electrical techniques. This technique only requires the fabrication of three types of devices: electron-only, hole-only, and double-carrier device. (Fig. 2.7) By

separately investigating the hole (electron) current density, $J_{p(n)}$, and double-carrier current, J_D,

$$\gamma_{pre} = \frac{16\pi}{9} \frac{J_p J_n}{J_D^2 - (J_p + J_n)^2} \tag{2.50}$$

where J_D is obtained from double-carrier current in the injected-plasma (IP) limit, J_{IP},

$$J_{IP} = \left(\frac{9}{8}\pi\right)^{1/2} \varepsilon \left[\frac{2\mu_p \mu_n}{\gamma_{pre}}\right]^{1/2} \frac{V^2}{L^3} \tag{2.51}$$

and the current in the infinite recombination limit of two single-carrier, space-charge-limited diodes placed back-to-back, J_{BB},

$$J_{BB} = \frac{9}{8} \varepsilon (\mu_p + \mu_n) \frac{V^2}{L^3} \tag{2.52}$$

This technique also offers unique advantages such as it reflects actual device conditions and it is not limited by resistive-capacitative (RC) effect.

2.3.4 Transient Photovoltage/Photocurrent Measurement

While the aforementioned measurements are carried out under short-circuit conditions, the recombination and transport in OPV can be strongly dependent on external bias. The transient photovoltage/photocurrent measurements offer a convenient solution to predict transport at and near V_{oc} [83, 84]. The measurement setup uses a white light bias to control the carrier density, where a short pulse of excitation light is incident to create additional carriers. The carrier lifetime is obtained from photovoltage transient at open circuit conditions.

Li et al. [85] used transient photovoltage techniques to investigate the different recombination mechanisms in polymer/fullerene, polymer/polymer and polymer/nanocrystal solar cell systems. The transient photovoltage decay kinetics is fitted by either a single-exponential fit or higher-order-exponential fits:

$$\delta V = A_1 \exp\left(-\frac{t}{\tau_1}\right) + A_1 \exp\left(-\frac{t}{\tau_2}\right) + \ldots \tag{2.53}$$

They discovered that while P3HT/$PC_{61}BM$ devices follows mono-exponential fit, suggesting that bimolecular recombination is the dominant recombination process. However, polymer/polymer and polymer/nanocrystal solar cell obey higher-order-exponential fit. This could be due to the presence of other recombination mechanisms in these systems.

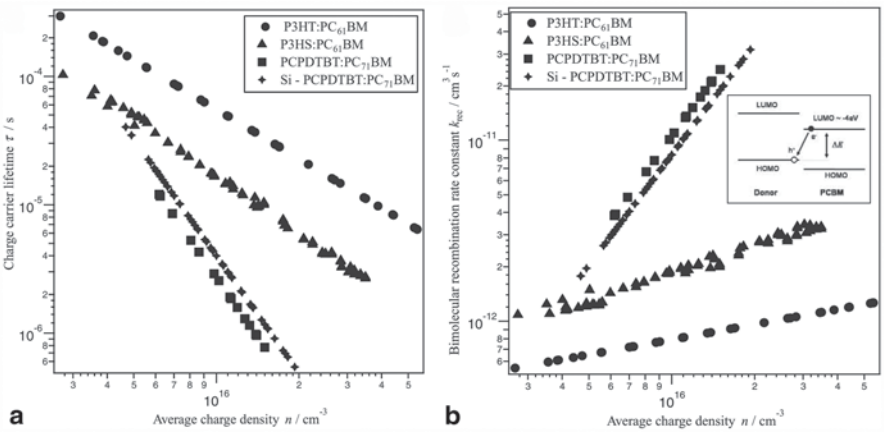

Fig. 2.8 **a** Carrier lifetimes as a function of average charge density for four different BHJ devices, **b** The corresponding bimolecular recombination rate constant (k_{rec}) as a function of carrier density, n. The inset shows the bimolecular recombination process

It is often useful to obtain a direct relationship between carrier density and carrier lifetime. For this purpose, transient photovoltage measurement is often used in combination with charge extraction measurements. In 2008, Shuttle et al. [86] used a combination of transient photocurrent and transient photovoltage measurements using the same pulsed light intensity. Specifically, the amount of charge introduced by the pulsed laser light, ΔQ, is determined by integrating short-circuit current with respect to time. The differential capacitance is obtained by $C = \Delta Q / \Delta V$, where ΔV is the voltage change at open circuit when the device is exposed to the same intensity of laser pulse. Therefore, the carrier density can be determined by:

$$n = \frac{1}{eAd} \int_0^{V_{oc}} C \mathrm{d}V \tag{2.54}$$

where A is the device area, e is the electronic charge and d is the thickness of the active layer.

Maurano et al. [87] and Shuttle et al. [38] later also demonstrate a charge extraction (CE) technique to extract carrier density information along with transient photovoltage measurement. They found that the V_{oc} of P3HT:PCBM photovoltaic devices can be influenced not only by their relative energetic levels, but also by trap-limited bimolecular recombination of free-charge carriers at the P3HT:PCBM interface. Maurano [87] and later Guo et al. [17] demonstrated that the charge density and V_{oc} follows an exponential relationship: $n = n_0 e^{\gamma V_{oc}}$, where n is the carrier density and γ is a constant. In addition, the charge carrier lifetimes obey a power law relationship with charge density: $\tau = \tau_0 n^{-\lambda}$, where τ is the carrier lifetime and λ is a constant. The values of γ and λ are extracted by plotting n and τ against varying V_{oc} (controlled by bias intensity) and n, respectively. Furthermore, the recombination rate constant, k_{rec}, is calculated from $k_{rec} = 1/(\lambda + 1) n\tau(n)$. The relationship between V_{oc} and k_{rec} can be a powerful tool to diagnose the interface recombination kinetics and help optimize the voltage output of OPVs (Fig. 2.8).

2.3.5 Charge Extraction by Linearly Increasing Voltage (CELIV) and Photo-CELIV Measurement

CELIV technique has been widely used for low-mobility materials such as organic semiconductors [88–96]. It allows measuring film with high-bulk conductivity and studying the relaxation of the photogenerated charge carriers in the density-of-states (DOS). Therefore, the time-dependent carrier mobility and concentration of the photogenerated charge carriers can be experimentally measured simultaneously from the current transients [46, 69, 97].

In CELIV experiments, a linearly increasing voltage pulse with a slope $A = U/t_{pulse}$ is applied to the sample to extract the equilibrium charge carriers. (Fig. 2.9) If the light pulse is used to photogenerate the charge carriers, the linearly increasing voltage pulse starts after some delay time t_{del}. Next, the current increases due to the conductivity current (Δj) caused by the charge carriers transported in the film. The current continues to increase as the voltage increases until the charge carriers are extracted from the film and the current drops down to the capacitive step if the duration of the applied pulse is long enough and there is no carrier injection from the contacts.

I. In the low conductivity case, when $\tau_\sigma \gg t_{tr}$ or $(\Delta j \ll j(0))$, where Δj is the current related to the conductivity of the film, τ_σ is the dielectric relaxation time, and $j(0)$ is the capacitive step of the current. The charge carrier mobility can be estimated as:

$$\mu = K\frac{d^2}{At_{max}^2} \tag{2.55}$$

where $K = 2/3$ for volume and $K = 2$ for surface photogeneration, t_{max} is maximum current

II. Medium conductivity, when,

$$\tau_\sigma = t_{tr}$$

$$\mu = \frac{2d^2}{3At_{\max}^2\left[1 + 0.36\dfrac{\Delta j}{j(0)}\right]} \tag{2.56}$$

where $1 + 0.36\dfrac{\Delta j}{j(0)}$ is a correction factor.

III. High conductivity: when when $\tau_\sigma \gg t_{tr}$ (or) $\Delta j \gg j(0)$, the charge carrier mobility can be estimated as:

$$\mu = \frac{d\tau_\sigma}{At_{max}^3} = \frac{d^2 j(0)}{At_{max}^2 \Delta j} \tag{2.57}$$

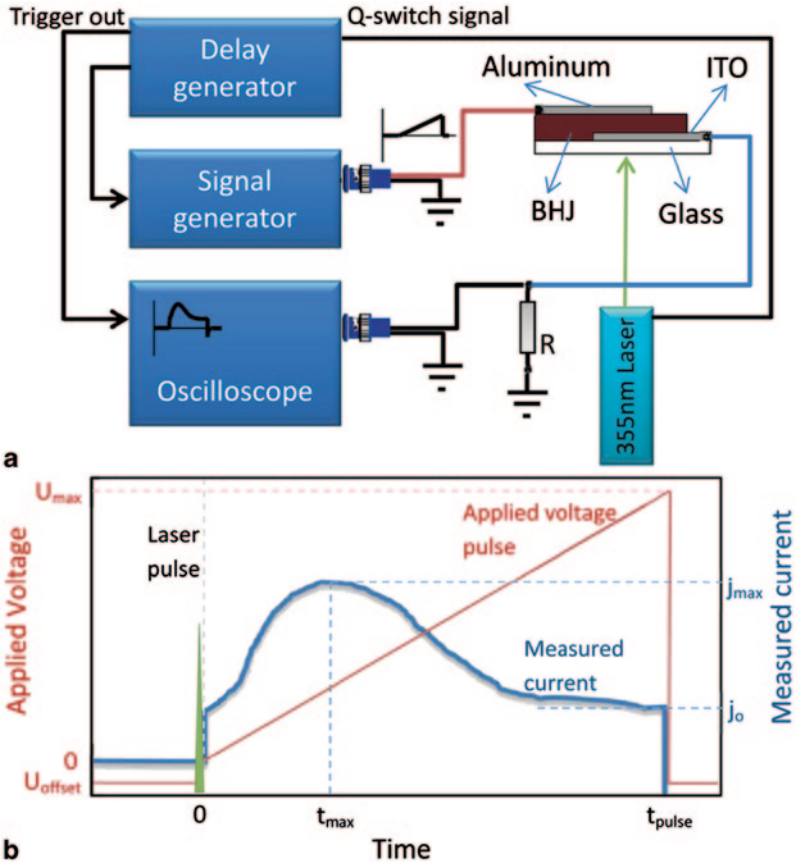

Fig. 2.9 Schematics of experimental setups and current transient signals for the photo-CELIV technique: **a** a laser pulse is used to photogenerate free carriers in the device. The laser Q-switch is synchronized with the applied triangle pulse by a delay generator, **b** applied triangle voltage pulse and current transient response in photo-CELIV. The triangle voltage is described by pulse length t_{pulse} and amplitude U_{max}. A small offset voltage, U_{offset}, is applied to compensate the internal electric field, t_{max} is defined as the time to reach the maximum extracted current and it corresponds to the photogenerated charge carrier transit time and mobility. j_0 is the displacement charging current, which is used to estimate the device capacitance or film thickness

The constant offset voltage has severe drawbacks. As it is already applied before laser excitation, charge carriers are injected into the bulk of the solar cell. These injected charge carriers may interact with photogenerated charge carriers before they are both extracted. Moreover, a constant offset voltage disregards the fact that the open-circuit voltage decreases due to charge carrier recombination. Therefore, Baumann et al. [91], instead of photo-CELIV, they account for the decrease in the charge carrier density and thus in Voc by applying a time-dependent offset voltage to the solar cell during the delay time. The experiment can be divided as three time ranges: (a) charge carrier generation, (b) charge carrier recombination, and (c)

charge carrier extraction. First, charge carriers are generated by a shortlaser flash and extracted after certain time delay by a triangular voltage pulse. During the delay time, a constant offset voltage is applied to the solar cell in order to compensate the internal electrical field, so that the charge carriers are mostly hindered to leave the device prior to charge extraction, and recombine instead.

By performing this measurement, they avoid the sweep-out of charge carriers during the delay time. A two-step approach is used where V_{oc} transient is independently acquired to allow all charge carriers recombine by the use of a high-impedance resistor (G_{Ohm}) and V_{oc} transient is obtained by switching-off the excitation light. In the second step, the acquired Voc transient is used as the time-dependent offset voltage, which is applied to the solar cell to adaptively suppress current flow in the external circuit during the time range. Thus, an untimely charge injection or extraction is avoided.

2.3.6 Microwave Conductivity

Recently, microwave measurement has been reported by several groups to study the local mobility of varies organic semiconductor systems [98–102]. Comparing to TOF method that due to the presence of domain boundaries or defects, mobility values sometime cannot be determined accurately at the molecular scale. As mentioned earlier, the active layer for TOF measurements is typically much thicker than for preparing solar cells, which may cause differences in morphology in the vertical direction. Meanwhile, photo-CELIV measurement is also limited by Ohmic contacts and possible neglect of faster OPV charge transport process [99]. On the other hand, TRMC is a contactlessmeasurement technique, avoiding the necessity to apply Ohmic contacts and eliminate the issues with interfaces between active layers and electrodes. This could be beneficial for predict-ing device performance without the fabrication of actual devices [9]. Meanwhile, TRMC provides nanosecond time scale resolution which is superior than typical photo-CELIV. In principle, TRMC is a high-frequency AC measurement utilizing continuous X-band microwaves. Due to the rapid change of the direction of the electric field, the drift distance for charge movement is relatively small (~nm), thus not able to pass domain boundaries. These mobilities are more "intrinisic" comparing to those obtained using photo-CELIV, TOF, or other DC techniques

However, TRMC does not differentiate the electron and hole mobilites. The technique simply measures the change in conductivity, given by: $\Delta\sigma$, given by:

$$\Delta\sigma = e\sum_i n_i \mu_i \tag{2.58}$$

In which n_i is the photoinduced change in concentration; μ_i is the corresponding mobility of charge carrier; and e is the electronic charge.

During the formation of mobile charges in BHJ blends, the yield for mobile charge carrier generation was related to the Gibbs energy (ΔG_{CS}) involved in the exciton in the exciton dissociation process.

In principle, TRMC involves the monitoring of change in the conductance of sample upon flash photolysis, ΔG based on the normalized change in the microwave power, $\Delta P / P$:

$$-\frac{\Delta P}{P} = K\Delta G \tag{2.59}$$

Assuming a single-charge-carrier pair generated by every photon, the change in conductivity can be simplified as:

$$\Delta\sigma = en\sum_i \mu_i = en(\mu_e + \mu_h) \tag{2.60}$$

Thus ΔG can be represented as:

$$\Delta G = \beta e \sum \mu \int_0^L n_p(z)dz \tag{2.61}$$

where $n_p(z)$ is the concentration at a depth z within the active layer with a thickness L, β is the ratio between long and short internal dimensions of the waveguide.

In characterizing organic semiconductor, TRMC has been used to identify short-range intramolecular mobilities to establish structure-transport relationships. In OPV configurations, TRMC is used to evaluate film processing conditions. For example, Saeki et al. [102] developed a Xe-flash TRMC with a white-light pulse to identify the optimal D/A blend ratios without fabrication of the actual devices. In their study, a number of high-performance systems are compared at varying PCBM content. They found that the PCE/V_{oc} is correlated with $\Delta\sigma_{max}$ for PBDTTT-CF:PCBM system. However, in contrast to the steady state *I*-*V* measurement which generates a linear dependence: $J_{sc} \propto P^{\alpha}$ with α value close to unity, the TRMC shows a sublinear dependence. By correlating the TRMC mobility and DC mobility, $\mu_{TRMC} \approx \beta(\mu_{Dc})$.

TRMC has been successfully used to study the morphology and charge transport behavior based on donor:acceptor mixing. In the study of pBTTT:$PC_{71}BM$ systems with different PCBM loading by Rance et al. [103], dependence of $\varphi\Sigma\mu$ on the PCBM loading is shown in Fig. 2.10. At low PCBM loading, (<50 wt%) which involves the presence of polymer:PCBM mixed region, $\varphi\Sigma\mu$ is relatively small. Interestingly, with higher PCBM loading exceeding 1:1, a drastic enhancement in $\varphi\Sigma\mu$ is observed. Since higher PCBM loading does not significantly alter the electron generation rate, this is rather due to the formation of pure PCBM region which enhances the electron mobility, $\Sigma\mu$. This indicates that the charges can escape the mixed phase before recombination occurs. However, when using nonintercalating bis-PCBM as the acceptor component with pBTTT, $\varphi\Sigma\mu$ shows little dependence on fullerene loading, which indicates the relative strong-phase separation behavior

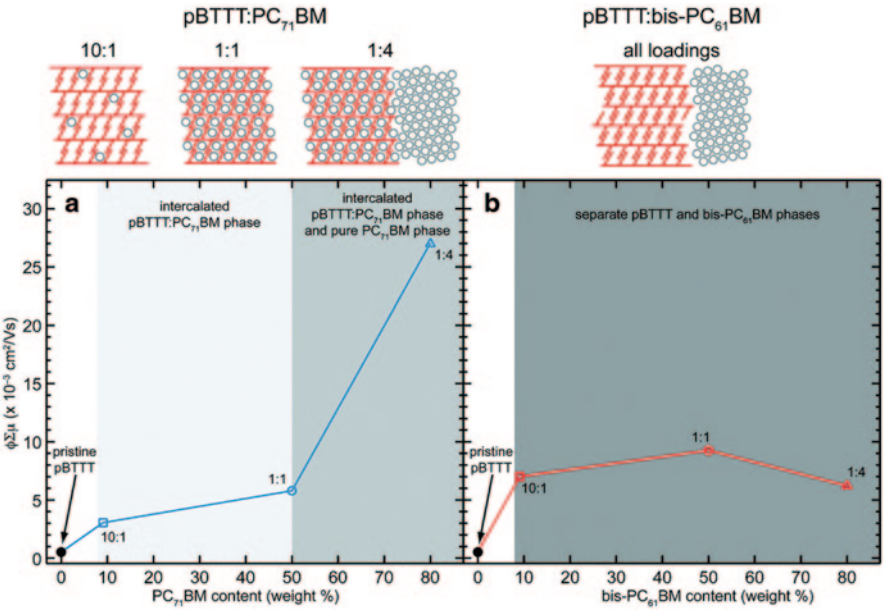

Fig. 2.10 Yield mobility $\varphi\Sigma\mu$ product plotted versus fullerene content for blends of pBTTT either **a** the intercalated $PC_{71}BM$ phase or **b** the nonintercalated bis-$PC_{61}BM$ phase; the points were taken at an absorbed photon flux of ~10^{12} photon/cm^2/pulse. Reproduced from ref [103]

in this system, thus it requires the diffusion of excitons to the interface between relatively pure polymer and fullerene domains. Ferguson et al. [104] also demonstrated that at low PCBM loading below capable of electron transport in actual devices (percolation threshold), the mobilities of PCBM can be closely monitored. This study demonstrates that TRMC has its unique advantages over several device-based measurement where successful hole/electron transport to the contacts has to be ensured. By further calculating the frequency-dependent mobility, TRMC techniques can be useful in studying cluster sizes [99, 104].

By exciting the photoactive blend at different wavelengths, the relationship between excess Gibbs energy, ΔG_{CS}, and carrier quantum yield can be studied [105, 106]. Murthy et al. [105] used 500 and 830 nm excitation wavelengths and found that $\varphi\Sigma\mu$ shows negligible difference at low-incidence intensity. Since $\Sigma\mu$ is not directly related to excitation wavelength, they concluded that the excess energy as a result of higher-energy photon does not lead to the increase of quantum yield, φ. By comparing the intensity normalized photoconductance action spectra of P3HT:PCBM and P3HT:bisPCBM active layers, a shift of ΔG onset can be observed. This result serves a direct proof of smaller electron affinity of bis-PCBM comparing to PCBM [107].

2.4 Outlook

In this chapter, we have discussed briefly on the charge transport and recombination in organic semiconductors. We further extended this discussion to the fundamental operation principles in OPV devices. Specifically, the origins of V_{oc}, J_{sc}, and FF, as well as the two fundamental recombination mechanisms: geminate and nongeminate recombination. Next, we focused on the various experimental techniques such as TOF, OFET, SCLC, transient photovoltage/photocurrent, CELIV/photo-CELIV, TRMC, etc., which are widely employed by the community to measure charge transport and recombination processes. Reducing both geminate and nongeminate recombination are key issues to further improve the PCE of OPVs. Therefore, correlating device physics measurements can establish the missing link between the chemical structure, morphology, and the resulting device performance and provide key information for optimizing device parameters.

Reference

1. Coropceanu, V. *et al.* Charge transport in organic semiconductors. *Chemical Reviews* **107**, 926–952, doi:10.1021/cr050140x (2007).
2. Shuai, Z., Geng, H., Xu, W., Liao, Y. & Andre, J.-M. From charge transport parameters to charge mobility in organic semiconductors through multiscale simulation. *Chemical Society Reviews* **43**, 2662–2679, doi:10.1039/C3CS60319A (2014).
3. Horowitz, G. Organic field-effect transistors. *Advanced Materials* **10**, 365–377, doi:10.1002/(sici)1521–4095(199803)10:5<3.0.co;2-u (1998).
4. Borsenberger, P. M., Pautmeier, L. & Bassler, H. CHARGE TRANSPORT IN DISORDERED MOLECULAR-SOLIDS. *Journal of Chemical Physics* **94**, 5447–5454, doi:10.1063/1.460506 (1991).
5. Schoonveld, W. A., Vrijmoeth, J. & Klapwijk, T. M. Intrinsic charge transport properties of an organic single crystal determined using a multiterminal thin-film transistor. *Applied Physics Letters* **73**, 3884–3886, doi:10.1063/1.122924 (1998).
6. Meijer, E. J., Matters, M., Herwig, P. T., de Leeuw, D. M. & Klapwijk, T. M. The Meyer-Neldel rule in organic thin-film transistors. *Applied Physics Letters* **76**, 3433–3435, doi:10.1063/1.126669 (2000).
7. Kippelen, B. & Brédas, J.-L. Organic photovoltaics. *Energy & Environmental Science* **2**, 251, doi:10.1039/b812502n (2009).
8. Brenner, T. J. K., Hwang, I., Greenham, N. C. & McNeill, C. R. Device physics of inverted all-polymer solar cells. *Journal of Applied Physics* **107**, 114501, doi:10.1063/1.3371364 (2010).
9. Bisquert, J. & Garcia-Belmonte, G. On Voltage, Photovoltage, and Photocurrent in Bulk Heterojunction Organic Solar Cells. *Journal of Physical Chemistry Letters* **2**, 1950–1964, doi:10.1021/jz2004864 (2011).
10. Scharber, M. C. & Sariciftci, N. S. Efficiency of bulk-heterojunction organic solar cells. *Progress in Polymer Science* **38**, 1929–1940, doi:10.1016/j.progpolymsci.2013.05.001 (2013).
11. Qi, B. & Wang, J. Open-circuit voltage in organic solar cells. *Journal of Materials Chemistry* **22**, 24315–24325, doi:10.1039/c2jm33719c (2012).
12. Cowan, S. R., Roy, A. & Heeger, A. J. Recombination in polymer-fullerene bulk heterojunction solar cells. *Physical Review B* **82**, 245207 (2010).

13. Vandewal, K., Tvingstedt, K., Gadisa, A., Inganäs, O. & Manca, J. V. Relating the open-circuit voltage to interface molecular properties of donor:acceptor bulk heterojunction solar cells. *Physical Review B* **81**, 125204 (2010).
14. Wetzelaer, G.-J. A. H., Kuik, M. & Blom, P. W. M. Identifying the Nature of Charge Recombination in Organic Solar Cells from Charge-Transfer State Electroluminescence. *Advanced Energy Materials* **2**, 1232–1237, doi:10.1002/aenm.201200009 (2012).
15. Wetzelaer, G.-J. A. H., Kuik, M., Lenes, M. & Blom, P. W. M. Origin of the dark-current ideality factor in polymer:fullerene bulk heterojunction solar cells. *Applied Physics Letters* (2011).
16. Yamamoto, S., Orimo, A., Ohkita, H., Benten, H. & Ito, S. Molecular Understanding of the Open-Circuit Voltage of Polymer:Fullerene Solar Cells. *Advanced Energy Materials* **2**, 229–237, doi:10.1002/aenm.201100549 (2012).
17. Guo, X. *et al.* Polymer solar cells with enhanced fill factors. *Nat Photon* **7**, 825–833, doi:10.1038/nphoton.2013.207 http://www.nature.com/nphoton/journal/v7/n10/abs/nphoton.2013.207.html#supplementary-information (2013).
18. Dibb, G. F. A., Kirchartz, T., Credgington, D., Durrant, J. R. & Nelson, J. Analysis of the Relationship between Linearity of Corrected Photocurrent and the Order of Recombination in Organic Solar Cells. *Journal of Physical Chemistry Letters* **2**, 2407–2411, doi:10.1021/jz201104d (2011).
19. Mihailetchi, V. D., Xie, H. X., de Boer, B., Koster, L. J. A. & Blom, P. W. M. Charge Transport and Photocurrent Generation in Poly(3-hexylthiophene): Methanofullerene Bulk-Heterojunction Solar Cells. *Advanced Functional Materials* **16**, 699–708, doi:10.1002/adfm.200500420 (2006).
20. Li, G., Zhu, R. & Yang, Y. Polymer solar cells. *Nat Photon* **6**, 153–161 (2012).
21. Green, M. A. Solar cell fill factors: General graph and empirical expressions. *Solid-State Electronics* **24**, 788–789, doi:http://dx.doi.org/10.1016/0038–1101(81)90062–9 (1981).
22. Kirchartz, T., Pieters, B. E., Kirkpatrick, J., Rau, U. & Nelson, J. Recombination via tail states in polythiophene:fullerene solar cells. *Physical Review B* **83**, 115209 (2011).
23. Street, R. A., Schoendorf, M., Roy, A. & Lee, J. H. Interface state recombination in organic solar cells. *Physical Review B* **81**, 205307 (2010).
24. Mauer, R., Howard, I. A. & Laquai, F. Effect of Nongeminate Recombination on Fill Factor in Polythiophene/Methanofullerene Organic Solar Cells. *The Journal of Physical Chemistry Letters* **1**, 3500–3505, doi:10.1021/jz101458y (2010).
25. Proctor, C. M., Kim, C., Neher, D. & Nguyen, T.-Q. Nongeminate Recombination and Charge Transport Limitations in Diketopyrrolopyrrole-Based Solution-Processed Small Molecule Solar Cells. *Advanced Functional Materials* **23**, 3584–3594, doi:10.1002/adfm.201202643 (2013).
26. Qi, B. & Wang, J. Fill factor in organic solar cells. *Physical Chemistry Chemical Physics* **15**, 8972–8982, doi:10.1039/c3cp51383a (2013).
27. Servaites, J. D., Yeganeh, S., Marks, T. J. & Ratner, M. A. Efficiency Enhancement in Organic Photovoltaic Cells: Consequences of Optimizing Series Resistance. *Advanced Functional Materials* **20**, 97–104, doi:10.1002/adfm.200901107 (2010).
28. Gonzalez-Rabade, A., Morteani, A. C. & Friend, R. H. Correlation of Heterojunction Luminescence Quenching and Photocurrent in Polymer-Blend Photovoltaic Diodes. *Advanced Materials* **21**, 3924-+, doi:10.1002/adma.200901114 (2009).
29. Baranovskii, S. D., Wiemer, M., Nenashev, A. V., Jansson, F. & Gebhardt, F. Calculating the Efficiency of Exciton Dissociation at the Interface between a Conjugated Polymer and an Electron Acceptor. *Journal of Physical Chemistry Letters* **3**, 1214–1221, doi:10.1021/jz300123k (2012).
30. Onsager, L. Deviations from Ohm's Law in Weak Electrolytes. *The Journal of Chemical Physics* **2**, 599–615, doi:doi:http://dx.doi.org/10.1063/1.1749541 (1934).
31. Braun, C. L. Electric field assisted dissociation of charge transfer states as a mechanism of photocarrier production. *The Journal of Chemical Physics* **80**, 4157–4161, doi:doi:http://dx.doi.org/10.1063/1.447243 (1984).

32. Deibel, C., Strobel, T. & Dyakonov, V. Origin of the Efficient Polaron-Pair Dissociation in Polymer-Fullerene Blends. *Physical Review Letters* **103**, 036402 (2009).
33. Groves, C., Blakesley, J. C. & Greenham, N. C. Effect of Charge Trapping on Geminate Recombination and Polymer Solar Cell Performance. *Nano Letters* **10**, 1063–1069, doi:10.1021/nl100080r (2010).
34. Groves, C. Suppression of geminate charge recombination in organic photovoltaic devices with a cascaded energy heterojunction. *Energy & Environmental Science* **6**, 1546–1551, doi:10.1039/c3ee24455e (2013).
35. Groves, C. Developing understanding of organic photovoltaic devices: kinetic Monte Carlo models of geminate and non-geminate recombination, charge transport and charge extraction. *Energy & Environmental Science* **6**, 3202–3217, doi:10.1039/c3ee41621f (2013).
36. Street, R. A., Cowan, S. & Heeger, A. J. Experimental test for geminate recombination applied to organic solar cells. *Physical Review B* **82**, 121301 (2010).
37. Clarke, T. M. *et al.* Charge carrier mobility, bimolecular recombination and trapping in polycarbazole copolymer:fullerene (PCDTBT:PCBM) bulk heterojunction solar cells. *Organic Electronics* **13**, 2639–2646, doi:10.1016/j.orgel.2012.07.037 (2012).
38. Shuttle, C. G., Hamilton, R., O'Regan, B. C., Nelson, J. & Durrant, J. R. Charge-density-based analysis of the current–voltage response of polythiophene/fullerene photovoltaic devices. *Proceedings of the National Academy of Sciences* **107**, 16448–16452, doi:10.1073/pnas.1004363107 (2010).
39. Zhang, Y., Dang, X. D., Kim, C. & Nguyen, T. Q. Effect of Charge Recombination on the Fill Factor of Small Molecule Bulk Heterojunction Solar Cells. *Advanced Energy Materials* **1**, 610–617, doi:10.1002/aenm.201100040 (2011).
40. Cowan, S. R., Banerji, N., Leong, W. L. & Heeger, A. J. Charge Formation, Recombination, and Sweep-Out Dynamics in Organic Solar Cells. *Advanced Functional Materials* **22**, 1116–1128, doi:10.1002/adfm.201101632 (2012).
41. Kirchartz, T. & Nelson, J. Meaning of reaction orders in polymer: fullerene solar cells. *Physical Review B* **86**, doi:10.1103/PhysRevB.86.165201 (2012).
42. Kirchartz, T., Pieters, B. E., Kirkpatrick, J., Rau, U. & Nelson, J. Recombination via tail states in polythiophene: fullerene solar cells. *Physical Review B* **83**, 13, doi:10.1103/PhysRevB.83.115209 (2011).
43. Wetzelaer, G.-J. A. H., Van der Kaap, N. J., Koster, L. J. A. & Blom, P. W. M. Quantifying Bimolecular Recombination in Organic Solar Cells in Steady State. *Advanced Energy Materials* **3**, 1130–1134, doi:10.1002/aenm.201300251 (2013).
44. Arumugam, S. *et al.* Charge transport in a two-dimensional molecular organic semiconductor. *Journal of Materials Chemistry C* **2**, 34–39, doi:10.1039/c3tc31670j (2014).
45. Morfa, A. J., Nardes, A. M., Shaheen, S. E., Kopidakis, N. & van de Lagemaat, J. Time-of-Flight Studies of Electron-Collection Kinetics in Polymer:Fullerene Bulk-Heterojunction Solar Cells. *Advanced Functional Materials* **21**, 2580–2586, doi:10.1002/adfm.201100432 (2011).
46. Pivrikas, A., Neugebauer, H. & Sariciftci, N. S. Charge Carrier Lifetime and Recombination in Bulk Heterojunction Solar Cells. *Ieee Journal of Selected Topics in Quantum Electronics* **16**, 1746–1758, doi:10.1109/jstqe.2010.2044978 (2010).
47. Pivrikas, A., Sariciftci, N. S., Juska, G. & Osterbacka, R. A review of charge transport and recombination in polymer/fullerene organic solar cells. *Progress in Photovoltaics* **15**, 677–696, doi:10.1002/pip.791 (2007).
48. Clarke, T. M., Jamieson, F. C. & Durrant, J. R. Transient Absorption Studies of Bimolecular Recombination Dynamics in Polythiophene/Fullerene Blend Films. *Journal of Physical Chemistry C* **113**, 20934–20941, doi:10.1021/jp909442 s (2009).
49. Clarke, T. M. *et al.* Non-Langevin bimolecular recombination in a silole-based polymer:PCBM solar cell measured by time-resolved charge extraction and resistance-dependent time-of-flight techniques. *Energy & Environmental Science* **5**, 5241–5245, doi:10.1039/c1ee02434e (2012).

50. Clarke, T. M. *et al.* Significantly Reduced Bimolecular Recombination in a Novel Silole-Based Polymer: Fullerene Blend. *Advanced Energy Materials* **1**, 1062–1067, doi:10.1002/aenm.201100390 (2011).
51. Gupta, D., Vidhyadhiraja, N. S. & Narayan, K. S. Transport of Photogenerated Charge Carriers in Polymer Semiconductors. *Proceedings of the Ieee* **97**, 1558–1569, doi:10.1109/jproc.2009.2019228 (2009).
52. Hoffmann, S. T. *et al.* How Do Disorder, Reorganization, and Localization Influence the Hole Mobility in Conjugated Copolymers? *Journal of the American Chemical Society* **135**, 1772–1782, doi:10.1021/ja308820j (2013).
53. Mauer, R., Howard, I. A. & Laquai, F. Effect of Nongeminate Recombination on Fill Factor in Polythiophene/Methanofullerene Organic Solar Cells. *Journal of Physical Chemistry Letters* **1**, 3500–3505, doi:10.1021/jz101458y (2010).
54. Mauer, R., Kastler, M. & Laquai, F. The Impact of Polymer Regioregularity on Charge Transport and Efficiency of P3HT:PCBM Photovoltaic Devices. *Advanced Functional Materials* **20**, 2085–2092, doi:10.1002/adfm.201000320 (2010).
55. Howard, I. A., Mauer, R., Meister, M. & Laquai, F. Effect of Morphology on Ultrafast Free Carrier Generation in Polythiophene:Fullerene Organic Solar Cells. *Journal of the American Chemical Society* **132**, 14866–14876, doi:10.1021/ja105260d (2010).
56. Marsh, R. A., Hodgkiss, J. M. & Friend, R. H. Direct Measurement of Electric Field-Assisted Charge Separation in Polymer: Fullerene Photovoltaic Diodes. *Advanced Materials* **22**, 3672-+, doi:10.1002/adma.201001010 (2010).
57. Finlayson, C. E. *et al.* Electronic Transport Properties of Ensembles of Perylene-Substituted Poly-isocyanopeptide Arrays. *Advanced Functional Materials* **18**, 3947–3955, doi:10.1002/adfm.200800943 (2008).
58. Zang, L., Che, Y. & Moore, J. S. One-Dimensional Self-Assembly of Planar π-Conjugated Molecules: Adaptable Building Blocks for Organic Nanodevices. *Accounts of Chemical Research* **41**, 1596–1608, doi:10.1021/ar800030w (2008).
59. Dabirian, R. *et al.* The Relationship between Nanoscale Architecture and Charge Transport in Conjugated Nanocrystals Bridged by Multichromophoric Polymers. *Journal of the American Chemical Society* **131**, 7055–7063, doi:10.1021/ja809731e (2009).
60. Balakrishnan, K. *et al.* Effect of Side-Chain Substituents on Self-Assembly of Perylene Diimide Molecules: Morphology Control. *Journal of the American Chemical Society* **128**, 7390–7398, doi:10.1021/ja061810z (2006).
61. Sohn, Y. & Stuckless, J. T. Characteristics of photoexcitations and interfacial energy levels of regioregular poly(3-hexythiophene −2,5-diyl) on gold. *Chemphyschem: a European journal of chemical physics and physical chemistry* **8**, 1937–1942, doi:10.1002/cphc.200700348 (2007).
62. Tautz, R. *et al.* Structural correlations in the generation of polaron pairs in low-bandgap polymers for photovoltaics. *Nature Communications* **3**, doi:10.1038/ncomms1967 (2012).
63. Proctor, C. M., Kim, C., Neher, D. & Thuc-Quyen, N. Nongeminate Recombination and Charge Transport Limitations in Diketopyrrolopyrrole-Based Solution-Processed Small Molecule Solar Cells. *Advanced Functional Materials* **23**, 3584–3594, doi:10.1002/adfm.201202643 (2013).
64. Zhang, Y., Liu, J. & Thuc-Quyen, N. Photoresponse of Donor/Acceptor Blends in Organic Transistors: A Tool for Understanding Field-Assisted Charge Separation in Small Molecule Bulk Heterojunction Solar Cells. *Acs Applied Materials & Interfaces* **5**, 2347–2353, doi:10.1021/am302833j (2013).
65. von Hauff, E., Dyakonov, V. & Parisi, J. Study of field effect mobility in PCBM films and P3HT:PCBM blends. *Solar Energy Materials and Solar Cells* **87**, 149–156, doi:http://dx.doi.org/10.1016/j.solmat.2004.06.014 (2005).
66. Lombardo, C., Danielson, E., Ooi, Z. E. & Dodabalapur, A. Lateral mobility measurements in organic bulk heterojunctions: comparison of field-effect and space charge mobilities. *Journal of Photonics for Energy* **2**, doi:10.1117/1.jpe.2.021007 (2012).

67. Labram, J. G., Kirkpatrick, J., Bradley, D. D. C. & Anthopoulos, T. D. Impact of Fullerene Molecular Weight on P3HT:PCBM Microstructure Studied Using Organic Thin-Film Transistors. *Advanced Energy Materials* **1**, 1176–1183, doi:10.1002/aenm.201100413 (2011).
68. Kumar, P., Jain, S. C., Kumar, V., Chand, S. & Tandon, R. P. Effect of illumination on the space charge limited current in organic bulk heterojunction diodes. *Applied Physics a-Materials Science & Processing* **94**, 281–286, doi:10.1007/s00339–008-4771–0 (2009).
69. Kokil, A., Yang, K. & Kumar, J. Techniques for characterization of charge carrier mobility in organic semiconductors. *Journal of Polymer Science Part B-Polymer Physics* **50**, 1130–1144, doi:10.1002/polb.23103 (2012).
70. Falzon, M.-F., Wienk, M. M. & Janssen, R. A. J. Designing Acceptor Polymers for Organic Photovoltaic Devices. *Journal of Physical Chemistry C* **115**, 3178–3187, doi:10.1021/jp110990w (2011).
71. Deng, Y. *et al.* Dithienocarbazole and Isoindigo based Amorphous Low Bandgap Conjugated Polymers for Efficient Polymer Solar Cells. *Adv Mater*, doi:10.1002/adma.201303586 (2013).
72. Dou, L. *et al.* Systematic investigation of benzodithiophene- and diketopyrrolopyrrole-based low-bandgap polymers designed for single junction and tandem polymer solar cells. *J Am Chem Soc* **134**, 10071–10079, doi:10.1021/ja301460 s (2012).
73. Lin, Y. *et al.* Small-Molecule Solar Cells with Fill Factors up to 0.75 via a Layer-by-Layer Solution Process. *Advanced Energy Materials*, n/a-n/a, doi:10.1002/aenm.201300626 (2013).
74. Min, J. *et al.* Alkyl Chain Engineering of Solution-Processable Star-Shaped Molecules for High-Performance Organic Solar Cells. *Advanced Energy Materials*, n/a-n/a, doi:10.1002/aenm.201301234 (2013).
75. Seri, M. *et al.* Fine Structural Tuning of Cyanated Dithieno[3,2-b:2′,3′-d]silole–Oligothiophene Copolymers: Synthesis, Characterization, and Photovoltaic Response. *Macromolecules* **46**, 6419–6430, doi:10.1021/ma4011186 (2013).
76. Massip, S. *et al.* Influence of Side Chains on Geminate and Bimolecular Recombination in Organic Solar Cells. *Journal of Physical Chemistry C* **115**, 25046–25055, doi:10.1021/jp2070584 (2011).
77. Carsten, B. *et al.* Examining the Effect of the Dipole Moment on Charge Separation in Donor-Acceptor Polymers for Organic Photovoltaic Applications. *Journal of the American Chemical Society* **133**, 20468–20475, doi:10.1021/ja208642b (2011).
78. Azimi, H., Senes, A., Scharber, M. C., Hingerl, K. & Brabec, C. J. Charge Transport and Recombination in Low-Bandgap Bulk Heterojunction Solar Cell using Bis-adduct Fullerene. *Advanced Energy Materials* **1**, 1162–1168, doi:10.1002/aenm.201100331 (2011).
79. Wetzelaer, G.-J. A. H. *et al.* Asymmetric electron and hole transport in a high-mobility n-type conjugated polymer. *Phys Rev B* (2012).
80. Bartelt, J. A. *et al.* The Importance of Fullerene Percolation in the Mixed Regions of Polymer-Fullerene Bulk Heterojunction Solar Cells. *Advanced Energy Materials* **3**, 364–374, doi:10.1002/aenm.201200637 (2013).
81. Zhou, N. *et al.* Morphology-Performance Relationships in High-Efficiency All-Polymer Solar Cells. *Advanced Energy Materials* **4**, n/a-n/a, doi:10.1002/aenm.201300785 (2014).
82. Faist, M. A. *et al.* Understanding the Reduced Efficiencies of Organic Solar Cells Employing Fullerene Multiadducts as Acceptors. *Advanced Energy Materials* **3**, 744–752, doi:10.1002/aenm.201200673 (2013).
83. O'Regan, B. C. *et al.* Measuring Charge Transport from Transient Photovoltage Rise Times. A New Tool To Investigate Electron Transport in Nanoparticle Films. *The Journal of Physical Chemistry B* **110**, 17155–17160, doi:10.1021/jp062761f (2006).
84. Hamilton, R. *et al.* Recombination in Annealed and Nonannealed Polythiophene/Fullerene Solar Cells: Transient Photovoltage Studies versus Numerical Modeling. *The Journal of Physical Chemistry Letters* **1**, 1432–1436, doi:10.1021/jz1001506 (2010).
85. Li, Z., Gao, F., Greenham, N. C. & McNeill, C. R. Comparison of the Operation of Polymer/Fullerene, Polymer/Polymer, and Polymer/Nanocrystal Solar Cells: A Transient Photocurrent and Photovoltage Study. *Advanced Functional Materials* **21**, 1419–1431, doi:10.1002/adfm.201002154 (2011).

86. Shuttle, C. G. *et al.* Experimental determination of the rate law for charge carrier decay in a polythiophene: Fullerene solar cell. *Applied Physics Letters* **92**, -, doi:http://dx.doi.org/10.1063/1.2891871 (2008).
87. Maurano, A. *et al.* Recombination Dynamics as a Key Determinant of Open Circuit Voltage in Organic Bulk Heterojunction Solar Cells: A Comparison of Four Different Donor Polymers. *Advanced Materials* **22**, 4987-+, doi:10.1002/adma.201002360 (2010).
88. Armin, A. et al. Doping-Induced Screening of the Built-in-Field in Organic Solar Cells: Effect on Charge Transport and Recombination. Advanced Energy Materials 3, 321–327, doi:10.1002/aenm.201200581 (2013).
89. Armin, A., Velusamy, M., Burn, P. L., Meredith, P. & Pivrikas, A. Injected charge extraction by linearly increasing voltage for bimolecular recombination studies in organic solar cells. *Applied Physics Letters* **101**, doi:10.1063/1.4747330 (2012).
90. Bange, S., Schubert, M. & Neher, D. Charge mobility determination by current extraction under linear increasing voltages: Case of nonequilibrium charges and field-dependent mobilities. *Physical Review B* **81**, doi:10.1103/PhysRevB.81.035209 (2010).
91. Baumann, A., Lorrmann, J., Rauh, D., Deibel, C. & Dyakonov, V. A New Approach for Probing the Mobility and Lifetime of Photogenerated Charge Carriers in Organic Solar Cells Under Real Operating Conditions. *Advanced Materials* **24**, 4381–4386, doi:10.1002/adma.201200874 (2012).
92. Baumann, A. *et al.* Influence of Phase Segregation on Recombination Dynamics in Organic Bulk-Heterojunction Solar Cells. *Advanced Functional Materials* **21**, 1687–1692, doi:10.1002/adfm.201002358 (2011).
93. Chellappan, V., Ng, G. M., Tan, M. J., Goh, W.-P. & Zhu, F. Imbalanced charge mobility in oxygen treated polythiophene/fullerene based bulk heterojunction solar cells. *Applied Physics Letters* **95**, doi:10.1063/1.3279135 (2009).
94. Juska, G., Nekrasas, N., Valentinavicius, V., Meredith, P. & Pivrikas, A. Extraction of photogenerated charge carriers by linearly increasing voltage in the case of Langevin recombination. *Physical Review B* **84**, doi:10.1103/PhysRevB.84.155202 (2011).
95. van der Hofstad, T. G. J. *et al.* Carrier Recombination in Polymer Fullerene Solar Cells Probed by Reversible Exchange of Charge between the Active Layer and Electrodes Induced by a Linearly Varying Voltage. *Journal of Physical Chemistry C* **117**, 3210–3220, doi:10.1021/jp306794j (2013).
96. Vijila, C. *et al.* Relation between charge carrier mobility and lifetime in organic photovoltaics. *Journal of Applied Physics* **114**, doi:10.1063/1.4829456 (2013).
97. Proctor, C. M., Kuik, M. & Thuc-Quyen, N. Charge carrier recombination in organic solar cells. *Progress in Polymer Science* **38**, 1941–1960, doi:10.1016/j.progpolymsci.2013.08.008 (2013).
98. Dicker, G., de Haas, M., Siebbeles, L. & Warman, J. Electrodeless time-resolved microwave conductivity study of charge-carrier photogeneration in regioregular poly(3-hexylthiophene) thin films. *Physical Review B* **70**, doi:10.1103/PhysRevB.70.045203 (2004).
99. Savenije, T. J., Ferguson, A. J., Kopidakis, N. & Rumbles, G. Revealing the Dynamics of Charge Carriers in Polymer:Fullerene Blends Using Photoinduced Time-Resolved Microwave Conductivity. *Journal of Physical Chemistry C* **117**, 24085–24103, doi:10.1021/jp406706u (2013).
100. Saeki, A., Fukumatsu, T. & Seki, S. Intramolecular Charge Carrier Mobility in Fluorene-Thiophene Copolymer Films Studied by Microwave Conductivity. *Macromolecules* **44**, 3416–3424, doi:10.1021/ma2004844 (2011).
101. Saeki, A., Tsuji, M. & Seki, S. Direct Evaluation of Intrinsic Optoelectronic Performance of Organic Photovoltaic Cells with Minimizing Impurity and Degradation Effects. *Advanced Energy Materials* **1**, 661–669, doi:10.1002/aenm.201100143 (2011).
102. Saeki, A. *et al.* A versatile approach to organic photovoltaics evaluation using white light pulse and microwave conductivity. *J Am Chem Soc* **134**, 19035–19042, doi:10.1021/ja309524f (2012).

103. Rance, W. L. *et al.* Photoinduced Carrier Generation and Decay Dynamics in Intercalated and Non-intercalated Polymer:Fullerene Bulk Heterojunctions. *ACS Nano* **5**, 5635–5646, doi:10.1021/nn201251v (2011).
104. Ferguson, A. J., Kopidakis, N., Shaheen, S. E. & Rumbles, G. Dark Carriers, Trapping, and Activation Control of Carrier Recombination in Neat P3HT and P3HT:PCBM Blends. *The Journal of Physical Chemistry C* **115**, 23134–23148, doi:10.1021/jp208014v (2011).
105. Murthy, D. H. K., Gao, M., Vermeulen, M. J. W., Siebbeles, L. D. A. & Savenije, T. J. Mechanism of Mobile Charge Carrier Generation in Blends of Conjugated Polymers and Fullerenes: Significance of Charge Delocalization and Excess Free Energy. *The Journal of Physical Chemistry C* **116**, 9214–9220, doi:10.1021/jp3007014 (2012).
106. Grzegorczyk, W. J. *et al.* Temperature-Independent Charge Carrier Photogeneration in P3HT−PCBM Blends with Different Morphology. *The Journal of Physical Chemistry C* **114**, 5182–5186, doi:10.1021/jp9119364 (2010).
107. Lenes, M. *et al.* Electron Trapping in Higher Adduct Fullerene-Based Solar Cells. *Advanced Functional Materials* **19**, 3002–3007, doi:10.1002/adfm.200900459 (2009).